Journal of Controlled Release 182 (2014) 83–89

Contents lists available at ScienceDirect

Journal of Controlled Release

journal homepage: www.elsevier.com/locate/jconrel

Characterizing EPR-mediated passive drug targeting using contrast-enhanced functional ultrasound imaging

Benjamin Theek [a], Felix Gremse [a], Sijumon Kunjachan [a], Stanley Fokong [a], Robert Pola [b], Michal Pechar [b], Roel Deckers [c], Gert Storm [d,e], Josef Ehling [a], Fabian Kiessling [a], Twan Lammers [a,d,e,*]

[a] Department of Experimental Molecular Imaging, University Clinic and Helmholtz Institute for Biomedical Engineering, RWTH-Aachen University, Aachen, Germany
[b] Institute of Macromolecular Chemistry, Academy of Sciences of the Czech Republic, Prague, Czech Republic
[c] Imaging Sciences Institute, University Medical Center Utrecht, Utrecht, The Netherlands
[d] Department of Pharmaceutics, Utrecht Institute for Pharmaceutical Sciences, Utrecht University, Utrecht, The Netherlands
[e] Department of Controlled Drug Delivery, MIRA Institute for Biomedical Technology and Technical Medicine, University of Twente, Enschede, The Netherlands

ARTICLE INFO

Article history:
Received 19 December 2013
Accepted 3 March 2014
Available online 12 March 2014

Keywords:
Drug targeting
Nanomedicine
Theranostics
Cancer
EPR
HPMA

ABSTRACT

The Enhanced Permeability and Retention (EPR) effect is extensively used in drug delivery research. Taking into account that EPR is a highly variable phenomenon, we have here set out to evaluate if contrast-enhanced functional ultrasound (ceUS) imaging can be employed to characterize EPR-mediated passive drug targeting to tumors. Using standard fluorescence molecular tomography (FMT) and two different protocols for hybrid computed tomography-fluorescence molecular tomography (CT-FMT), the tumor accumulation of a ~10 nm-sized near-infrared-fluorophore-labeled polymeric drug carrier (pHPMA-Dy750) was evaluated in CT26 tumor-bearing mice. In the same set of animals, two different ceUS techniques (2D MIOT and 3D B-mode imaging) were employed to assess tumor vascularization. Subsequently, the degree of tumor vascularization was correlated with the degree of EPR-mediated drug targeting. Depending on the optical imaging protocol used, the tumor accumulation of the polymeric drug carrier ranged from 5 to 12% of the injected dose. The degree of tumor vascularization, determined using ceUS, varied from 4 to 11%. For both hybrid CT-FMT protocols, a good correlation between the degree of tumor vascularization and the degree of tumor accumulation was observed, within the case of reconstructed CT-FMT, correlation coefficients of ~0.8 and *p*-values of <0.02. These findings indicate that ceUS can be used to characterize and predict EPR, and potentially also to pre-select patients likely to respond to passively tumor-targeted nanomedicine treatments.

1. Introduction

Upon i.v. administration, low-molecular-weight chemotherapeutic drugs generally present with suboptimal pharmacokinetics and with an inappropriate biodistribution. Due to their small size and/or their high hydrophobicity, for instance, systemically administered anticancer agents tend to have a short circulation half-life time and a large volume of distribution, resulting in low levels of accumulation in tumors and tumor cells, and in high concentrations in potentially endangered healthy tissues.

To improve the balance between the tumor accumulation and the off-target localization of chemotherapeutic drugs, and to thereby beneficially affect the balance between their efficacy and their toxicity, a large number of nanomedicine formulations have been designed and evaluated over the years [1–5]. Examples of clinically used tumor-targeted nanomedicines are liposomes, polymers, micelles, nanoparticles and antibodies. Several of these formulations have been approved for clinical use, including e.g. Doxil for ovarian cancer, breast cancer, multiple myeloma and Kaposi sarcoma, and Abraxane for breast cancer. Numerous other nanomedicines are currently in clinical trials, and a large number of additional formulations are under preclinical development [5,6].

The biodistribution of nanomedicine formulations is very different from that of low-molecular-weight drugs. As the size of nanocarrier materials generally is above the kidney clearance threshold (~5 nm), they tend to circulate for prolonged periods of time, and they are consequently able to exploit the fact that tumor blood vessels are more leaky than healthy blood vessels, resulting in passive, progressive and relatively selective accumulation at the pathological site over time. This phenomenon is known as the Enhanced Permeability and Retention (EPR) effect [7,8], and it is extensively used in drug delivery research. It is increasingly recognized, however, that EPR is a highly variably phenomenon, presenting not only with large differences between different animal models and patient tumors, but also with large inter- and intraindividual differences between tumors of the same sub-type. And

* Corresponding author at: Department of Experimental Molecular Imaging, RWTH Aachen University Clinic, Pauwelsstrasse 30, 52074 Aachen, Germany. Tel.: +49 241 80 36681; fax: +49 241 80 3380116.
E-mail address: tlammers@ukaachen.de (T. Lammers).

http://dx.doi.org/10.1016/j.jconrel.2014.03.007
0168-3659/

even within a single tumor, certain vessels are significantly more leaky than others. Several recent reviews critically describe and comprehensively discuss the validity and the variability of the EPR effect [9–14]. To better understand EPR, to predict which animal models or patient tumors are likely to benefit from EPR-mediated passive drug targeting, and to thereby individualize and improve nano-chemotherapeutic treatments, it therefore seems highly important to identify imageable parameters to characterize the EPR effect.

In recent years, tremendous progress has been made in developing (ever more) nanomedicine formulations. Only a few studies, however, have been undertaken to better understand the EPR effect, to identify the underlying pathophysiological parameters dictating EPR, and to develop imaging protocols to visualize and predict EPR. Even though it seems highly likely, for instance, that the degree of tumor vascularization (i.e. the relative vascular volume of tumors) correlates with the degree of EPR-mediated passive drug targeting, no experimental evidence for this has thus far been provided. Here, we therefore set out to visualize and quantify the tumor accumulation of near-infrared-fluorophore (NIRF) labeled polymeric drug carriers based on *N*-(2-hydroxypropyl)-methacrylamide (HPMA), and we correlated their EPR-mediated tumor accumulation with the degree of tumor vascularization, assessed using two different contrast-enhanced ultrasound (ceUS) imaging techniques.

HPMA copolymers are prototypic and routinely used macromolecular drug carriers, which have been extensively employed for EPR-mediated passive drug targeting [15–17]. As for other long-circulating nanocarriers, however, such as for liposomes, the tumor accumulation of HPMA copolymers varies quite considerably, both in animal models and in patients, from barely detectable, to up to 5% of the injected dose [18–21]. In spite of this conceptual shortcoming, HPMA copolymers have been extensively used over the years, to improve the tumor-directed delivery of many different low-molecular-weight drugs, including e.g. anthracyclines, antimetabolites, taxanes and platinates [15,16,22,23], and their biodistribution and target site accumulation have been detailedly documented upon labeling them with radionuclides, magnetic resonance contrast agents and fluorophores [24–28].

Preclinically, drug delivery systems generally work very well, with significant improvements in both target site accumulation and therapeutic efficacy. Clinically, however, due to the abovementioned large inter- and intraindividual variability in EPR, the efficacy of passively tumor-targeted nanomedicines is compromised, with often significant improvements in tolerability, but hardly any increases in efficacy [9, 10,14]. Consequently, there seems to be a clear need to develop methods to visualize and characterize the EPR effect, in order to preselect patients presenting with sufficiently high levels of EPR, to thereby (pre-) stratify responders and non-responders, and to thereby individualize and improve nano-chemotherapeutic treatments.

We here used ~70 kDa-sized near-infrared fluorophore (NIRF) -labeled HPMA copolymers (which are known to efficiently accumulate in subcutaneous CT26 tumors in mice via EPR [29]), hybrid computed tomography-fluorescence molecular tomography (CT-FMT; [30–32]) and microbubble (MB) -based contrast-enhanced functional ultrasound (ceUS) imaging [33,34], to demonstrate that the degree of tumor vascularization correlates with the degree of EPR-mediated passive drug targeting. These findings indicate that relatively easily imageable vascular parameters, such as tumor blood volume and tumor blood flow, can be used to characterize EPR, and to on the basis of this preselect patients likely to respond to passively tumor-targeted nanomedicine therapies.

2. Materials and methods

2.1. Materials

1-Aminopropan-2-ol, methacryloyl chloride, dichloromethane (DCM), sodium carbonate, glycylglycine (GG), 4,5-dihydrothiazole-2-thiol (TT), 2,2'-azobis(isobutyronitrile) (AIBN), 6-aminohexanoic acid (AH), N,N-dimethylformamide (DMF), N,N′-dicyclohexylcarbodiimide (DCC), dimethylsulfoxide (DMSO), N,N-diisopropylethylamide (DIPEA), Triton X-100, diethylether and methanol were purchased from Sigma-Aldrich, USA. N-Butylcyanoacrylate was purchased from Special Polymer Ltd., Bulgaria. The near-infrared fluorescent dyes Dy676 and Dy750 were purchased from Dyomics GmbH, Germany.

2.2. Polymer synthesis

The synthesis and characterization of pHPMA-Dy750 were performed as described in [32]. Briefly, the monomer *N*-(2-hydroxypropyl) methacrylamide (HPMA) was synthesized by the reaction of methacryloyl chloride with 1-aminopropan-2-ol in DCM using sodium carbonate. N-Methacyloyl glycylglycine was prepared by Schotten–Baumann acylation of glycylglycine with methacryloyl chloride in aqueous alkaline medium. 3-(*N*-methacryloyl glycylglycyl)thiazolidine-2-thione (Ma-GG-TT) was prepared by the reaction of Ma-GG-OH with 4,5-dihydrothiazole-2-thiol in DMF in the presence of DCC. The multivalent random copolymer precursor poly(HPMA-co-Ma-GG-TT) was prepared by solution radical copolymerization of HPMA (85 mol %) and Ma-GG-TT (15 mol %) in DMSO at 50 °C for 6 h. The concentration of monomers in the copolymerization mixture was 12.5% *w/w*, and that of the initiator AIBN was 1.5% *w/w*. The molecular weight of polymer precursor was 65 kDa, and its polydispersity index (M_W/M_N) was 1.7. The polymer precursor poly(HPMA-coMa-GG-TT) (0.39 mg, 0.78 mmol TT group per gram of polymer) was dissolved in methanol (0.6 ml). Dy750-NH_2 (1 mg; 1.26 μmol) and DIPEA (0.43 μL, 2.52 μmol) were added. After a 0.5 h reaction with the near-infrared fluorescent dye, the polymer was aminolyzed with 1-aminopropan-2-ol (5 μL). Fifteen minutes later, the aminolyzed copolymer was isolated by precipitation with diethylether, followed by centrifugation. The precipitate was dried under vacuum. Then, the dry copolymer was dissolved in water, purified by gel filtration on Sephadex G-25 in water (PD 10 column; Pharmacia), and freeze-dried, yielding 31 mg (80%) of poly(HPMA-co-Ma-GG-Dy750-co-Ma-GG-AP) (pHPMA-Dy750). The content of fluorescent dye was 2.5 wt%. The molecular weight and the polydispersity index of pHPMA-Dy750 were 67 kDa and 1.7, respectively.

2.3. Microbubble synthesis

Poly(butyl cyanoacrylate) (PBCA) -based microbubbles (MB) were synthesised as described in [35]. In brief, 3 ml of the monomer butyl cyanoacrylate were added drop-wise to an aqueous solution containing 1% (*w/v*) triton x-100 at pH 2.5. The mixture was subsequently agitated using an Ultra-turrax (IKA-Werke, Germany) at 10,000 rpm for 60 min, to obtain PBCA MB. The resulting MB suspension was subsequently purified by differential centrifugation, to obtain MB with a mean diameter of 2.2 ± 0.8 μm.

2.4. Animal experiments

All animal experiments were conducted according to the regulations of local and national committees for animal welfare. CD-1 nude mice (Charles River, Netherlands) were fed with chlorophyll-free food (to minimize the autofluorescence), kept in pathogen-free cages having their own ventilation, and placed in rooms with controlled 12 h light/dark cycles. Murine CT26 colon carcinoma cells were cultured in Dulbecco's modified Eagle's medium (DMEM; Gibco, Invitrogen, Germany), supplemented with 10% fetal bovine serum (FBS; Invitrogen, Germany) and 1% penicillin/streptomycin (10,000 U/ml penicillin; 10 mg/ml streptomycin, Invitrogen, Germany), at 37 °C and 5% CO_2 in a humid atmosphere. Tumor inoculation was performed by injecting 1×10^6 cells in 100 μl medium into the right flank. Tumors were allowed to grow for 10–12 days, until they reached a size of 6–8 mm in diameter.

2.5. Contrast-enhanced ultrasound (ceUS) imaging

During the whole measurement procedure, mice were inhalation-anaesthetized using 2% (*v*/*v*) isoflurane (which does not affect the cardiovascular system [36]). For functional US image acquisition, the Vevo2100 imaging system (VisualSonics, Canada) was used, in combination with an MS-250 US transducer, mounted on a motor stage to allow 3D measurements. The recording took place at a frequency of 21 MHz and 4% power. Before MB injection, a volumetric image acquisition with a step size of 0.1 mm (covering the whole tumor) was performed, to determine the background signal. Subsequently, 1×10^7 microbubbles were i.v. injected via a tail vein catheter. The injection phase was recorded in a central tumor slice allowing maximum intensity over time (MIOT) analysis. Immediately afterwards, a second 3D measurement was performed at the same settings, to determine the degree of tumor vascularization. Image analysis was performed as described below.

2.6. Hybrid computed tomography-fluorescence molecular tomography (CT-FMT)

The CT and FMT measurements were performed as in [32]. Mice i.v. injected with pHPMA-Dy750 or Dy676 (as a low-molecular-weight model drug) were positioned into a CT- and FMT-compatible mouse bed. They were then first scanned using dual energy Micro-CT (TomoScope 30s Duo, CT-Imaging, Germany), acquiring 720 projections containing 1032 × 1012 pixels in 1.1 full rotations within 90 s, upon which the volumetric data sets were reconstructed at an isotropic voxel size of 35 μm using a Feldkamp type algorithm and a smooth kernel. Subsequently, the mouse bed was transferred to the FMT (FMT 2500 LX, PerkinElmer, MA, USA), and FMT scans were performed at 680 and 750 nm using 115–120 grid points, arranged in a 3 × 3 mm grid.

2.7. Image analysis

Three different image analysis methods were employed. The first one, i.e. 'FMT only', is solely based on the 3D FMT data and a 2D reflectance image as it comes from the manufacturer (see Fig. 1). Using the TrueQuant software (PerkinElmer, MA, USA), an ellipsoid ROI was adjusted in the top view in two dimensions, and the depth was estimated by the user based on the visual signal. The other two analyses are both based on hybrid CT-FMT imaging protocols developed at our institute [32]. The 'CT-FMT fusion' protocol is based on the fusion of CT and FMT data sets by computing a rigid transformation using markers integrated into the mouse bed which are visible in both modalities [37]. For the 'CT-FMT recon & fusion' protocol the FMT raw data were reconstructed with an improved FMT reconstruction algorithm before fusing them with the CT data. The reconstructed CT images and FMT data, as well as the raw US data obtained using the Vevo2100 Imaging System, were analyzed using the Imalytics Preclinical software (Philips Research, Aachen, Germany). In case of the latter two analytical protocols, tumors were manually pre-segmented, by delineating the tumor margins in all three axes in the CT images. After this segmentation, the corresponding FMT data set was loaded as an image overlay, and the software computed the volume and fluorescence concentration for each segmented region. This information was used to determine the % of the injected dose (%ID) accumulating in tumors. Values were normalized to a tumor volume of 250 mm^3, as this was the average volume at the time point of analysis. Also for the determination of tumor vascularization two different protocols were applied. MIOT-based US analysis was performed as described in [38]. 3D B-mode data sets were analyzed in a manner similar to that employed in the CT-FMT analysis. Non-specific contrast noise was excluded. The difference in mean intensity of segmented tumors before and after MB injection was determined and assumed to be proportional to the degree of vascularization [39,40]. Furthermore the score was multiplied with a fixed and predetermined calibration factor, to yield reasonable and representative values in percentage. The correlation analysis is invariant to this calibration factor.

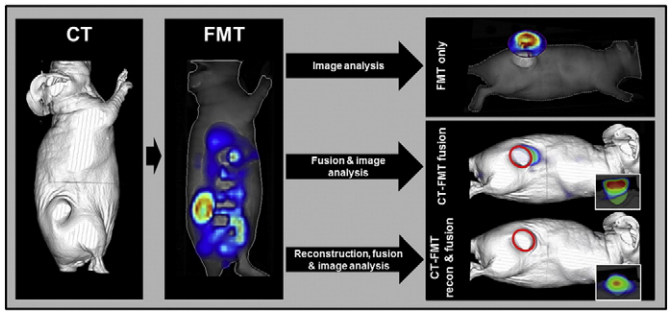

Fig. 1. Schematic overview of the FMT- and hybrid CT-FMT-based imaging protocols used. Mice were placed in a mouse bed compatible with the CT and the FMT imaging systems, and analyzed using both imaging techniques. FMT was employed to evaluate EPR-mediated drug targeting to tumors, and CT was used to provide anatomical information on tumor and mouse location and volume. Three different image analysis methods were applied to assess the tumor accumulation of pHPMA-Dy750, and to subsequently correlate this with the degree of tumor vascularization (as determined using two different US protocols; see Fig. 3).

2.8. Statistical analysis

The data was statistically analyzed using GraphPad Prism (Version 5.0). For correlation analysis, the coefficient of determination (r^2) was calculated. $P < 0.05$ was considered to represent statistical significance.

3. Results and discussion

To analyze EPR-mediated drug targeting to tumors, we used a ~10 nm-sized Dy750-labeled HPMA copolymer, and assessed its accumulation in subcutaneous CT26 tumors at 48 h post i.v. injection. The passive tumor accumulation of the NIRF-labeled polymer was visualized and quantified using three different optical imaging techniques, which we termed 'FMT-only', 'CT-FMT fusion' and 'CT-FMT recon & fusion' (Fig. 1). We furthermore used poly(butyl cyanoacrylate) (PBCA) -based microbubbles (MB) and contrast-enhanced US imaging to visualize and quantify the vascularization of tumors, and to correlate the degree of EPR-mediated drug targeting with the degree of tumor vascularization.

3.1. Optical imaging of EPR-mediated passive drug targeting

The use of optical imaging techniques to monitor the biodistribution and target site accumulation of nanomedicine formulations has increased exponentially in recent years [41–43]. It is therefore highly important to be aware of some of the limitations associated with these techniques, including e.g. the poor penetration depth of light (which particularly affects 2D FRI), and the lack of anatomical information (which affects both 2D FRI and 3D FMT). To resolve these issues, we have recently established a hybrid CT-FMT protocol, in which the anatomical information that can be obtained at very high resolution using micro-CT is fused with the functional/molecular information that can be obtained with very high sensitivity using FMT [32]. Furthermore, we developed a novel FMT reconstruction algorithm which resolves some of the drawbacks regarding anatomical information and light absorption by blood (i.e. by hemoglobin) in highly perfused organs and tissues.

In the present study, six different CT26 tumor-bearing mice were injected with pHPMA-Dy750, and imaged using standard FMT and hybrid CT-FMT. In addition, four mice were injected with the low-molecular weight model drug Dy676, to exemplify that EPR only occurs in case of nanomedicine formulations (see Fig. S1). Image analysis was

performed either with the TrueQuant software (in case of 'FMT only'), or with the Imalytics Preclinical software (in case of 'CT-FMT fusion' and 'CT-FMT recon & fusion'). As explained in the Materials and methods section, analyzing standard 3D FMT data sets suffers from several limitations, including the fact that the anatomical information that is conveyed in these analyses is solely based on a 2D reflectance image. As illustrated by the top right image in Fig. 1, the reconstructed 3D fluorescence signal (corresponding to probe accumulation in the tumor) is volume-rendered above a 2D reflectance image of the whole mouse, and one has to manually identify and select the tumor region-of-interest (ROI). This ROI can only be adjusted in two dimensions, i.e. length and width. Depth cannot be determined, and has to be estimated on the basis of the FMT signal. This approach consequently results in a relatively subjective interpretation of the data, and may give rise to biased, inaccurate and/or incorrect outcomes (depending on the observer's experience, expertise and expectations).

To address the shortcomings associated with standard FMT, we (and others) have developed protocols for the co-registration of CT and FMT data sets [30–32]. The advantage of such co-registered images is the addition of anatomical information, allowing for a much more precise 3D segmentation of tumors (and other organs of interest) on the basis of the CT images, yielding a highly reproducible method for biodistribution analyses [32]. In principle, upon co-registration, only signals which really are within the tumor volume are included in the quantitative analysis. As exemplified by the middle panels in Figs. 1 and 2, however, also the 'standard' CT-FMT fusion protocol has some drawbacks, as not all of the FMT-based optical signal coming from tumor and corresponding to the total tumor accumulation of pHPMA-Dy750 is covered by the (pre-) segmented CT tumor volume. In the middle right panel in Fig. 1, for instance, the red demarcation highlighting the CT-based tumor segmentation misses a significant portion of FMT-based nanocarrier signal coming from an area very close to the tumor. In the 2D and 3D analyses, this signal even appears to be coming from a region outside of the mouse (Fig. 2B), indicating that the standard FMT reconstruction algorithm leads to a significant misalignment of the signal. This either has the consequence of missing a relevant portion of the FMT signal, or requires a manual and highly subjective post-modification of the segmented area, fitting it to the signal most likely coming from the tumor. A recently developed algorithm takes the shape of the mouse into consideration, as well as the impact of light absorption by highly vascularized and/or highly perfused tissues, and thereby overcomes – at least in part – the abovementioned issues [30].

These insights are substantiated by Fig. 2, showing that in case of 'standard' CT-FMT fusion, a significant portion of the EPR-mediated nanocarrier accumulation in tumors is missed (~25% in this example; upon 3D analysis of the whole tumor). In Fig. 2A, a transversal slice of the CT image of the tumor region is depicted, with the tumor segmented in green. When subsequently fusing this image with the obtained FMT data, a large amount of the NIRF-labeled polymer passively accumulating in the tumor is found to be localized outside of the tumor ROI, and even outside of the whole mouse (Fig. 2B). When employing the recently developed CT-based FMT reconstruction, the optical signal is restrained to the volume (shape) of the mouse, and consequently appears completely within the tumor. As will be detailed below, both protocols for hybrid CT-FMT imaging, as well as standard FMT (i.e. 'FMT only'), were used to assess whether the degree of tumor vascularization correlates with the degree of EPR-mediated passive drug targeting.

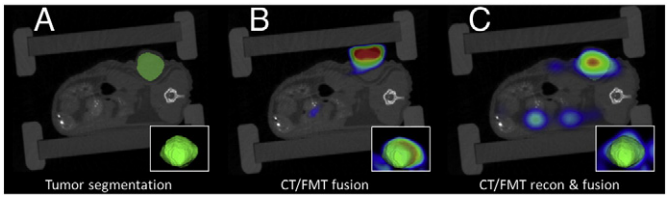

Fig. 2. CT-FMT imaging of EPR-mediated drug targeting to tumors. Panel A shows an anatomical CT images of a CT26 tumor-bearing mouse, imaged in 2D at the flank region, with the presegmented tumor depicted in green. 3D segmentations of the tumors are shown in the insets. In B and C, the CT signal is fused with the FMT signal, reporting on the EPR-mediated tumor accumulation of pHPMA-Dy750. In B, it can be seen that the CT-segmented tumor volume does not properly correspond with nanocarrier accumulation, with a significant portion of fluorescence generated by pHPMA-Dy750 present outside of the tumor (and outside of the whole mouse). In C, upon applying a CT-based FMT reconstruction protocol, which takes the shape of the mouse and its optical absorption properties into account, the nanocarrier signal properly colocalized with the tumor.

3.2. Contrast-enhanced ultrasound imaging of tumor vascularization

Using all three optical imaging protocols for quantitatively assessing the passive tumor accumulation of the NIRF-labeled polymeric drug carrier, we subsequently set out to determine the impact of tumor vascularization on the degree of EPR-mediated passive drug targeting. This is because it seems obvious that the more extensively vascularized tumors are, the more efficiently they can accumulate long-circulating nanomedicine formulations. Thus far, however, no experimental evidence has been provided for this seemingly logical assumption, and for this theranostic approach to preselect patients. To provide proof-of-principle for a correlation between the degree of tumor vascularization and the degree of EPR-mediated passive drug targeting, we correlated the tumor accumulation of pHPMA-Dy750 with the levels of tumor vascularization, determined using two different functional ceUS imaging protocols. The first ceUS imaging approach is based on maximal intensity over time (MIOT) analysis, acquiring information on tumor vascularization in 2D [38]. Both for preclinical and for clinical application, it would be convenient to assess tumor vascularization in 2D, as no motor stage or other comparable equipment is needed for temporally and spatially controlled image acquisition. However, as 2D measurements might not account for the large inter- and intra-individual variability typical of tumors, also 3D B-mode-based analyses were performed. The MIOT images in Fig. 3A depict the gradual contrast agent

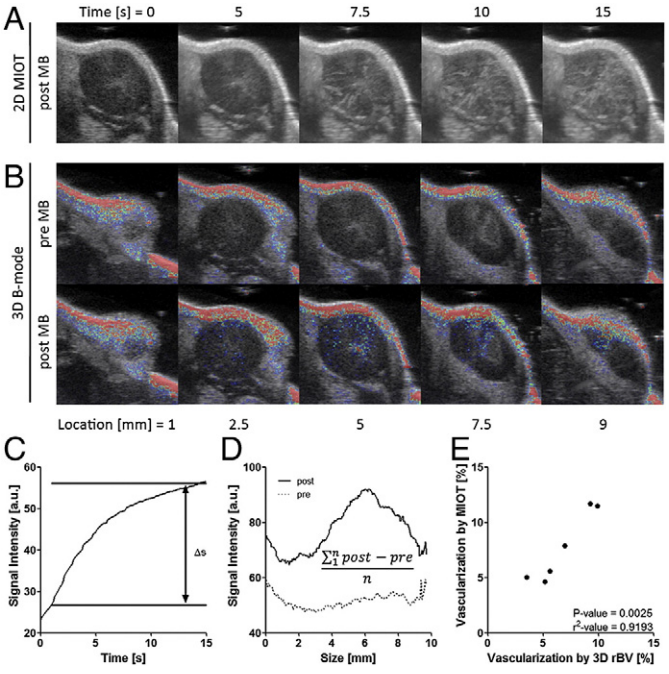

Fig. 3. Quantification of tumor vascularization using 2D MIOT and 3D B-mode US imaging. 2D maximal intensity over time (MIOT) images are depicted in A, and 3D B-mode images before and after microbubble administration are shown in B. Panel C exemplifies the cumulative 2D MIOT-based quantification of tumor vascularization, and panel D the assessment of tumor vascularization on the basis of subtracting post minus pre B-mode signal intensities. Panel E shows the correlation between 2D MIOT and 3D B-mode imaging.

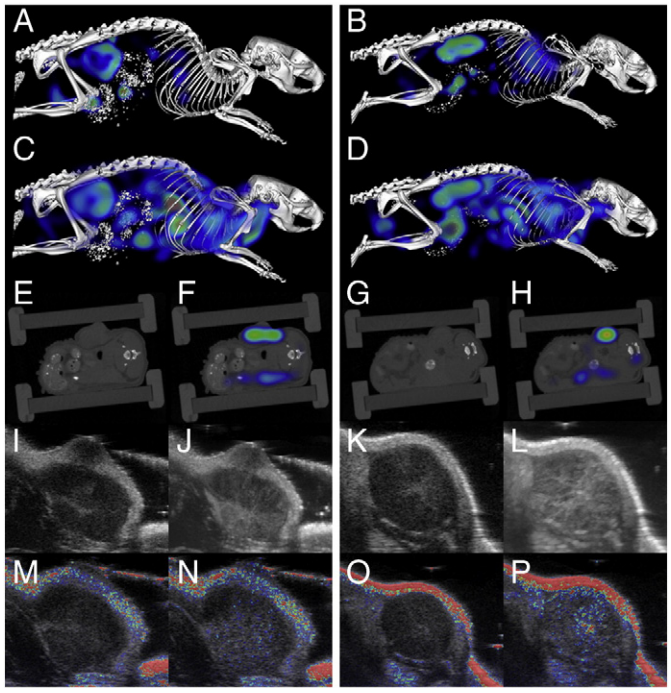

Fig. 4. Imaging EPR-mediated tumor targeting and tumor vascularization. The tumor accumulation of pHPMA-Dy750 was evaluated at 48 h post i.v. injection (A–H), and correlated with tumor vascularization (I–P). Standard (A–B) and reconstructed (C–H) CT-FMT images are shown for animals accumulating pHPMA-Dy750 to a relatively low (left panels; A, C) or high (right panels; B, D) extent. Tumor vascularization was assessed using 2D MIOT (I–L) and 3D B-mode US (M–P). The images clearly show that tumors which are well vascularized (right panels) accumulated the nanocarriers more efficiently than tumors which are less well-vascularized (left panels).

inflow over time. The difference in signal intensity between the onset of contrast agent inflow and the signal plateau is proportional to the degree of vascularization (Fig. 3C). Similarly, Fig. 3B shows 3D B-mode images of the tumor at different spatial locations, before and after contrast agent injection. The average of the mean signal intensity before and after contrast agent injection is also proportional to the degree of vascularization (Fig. 3D). Fig. 3E exemplifies that 2D MIOT and 3D B-mode analyses correspond relatively well.

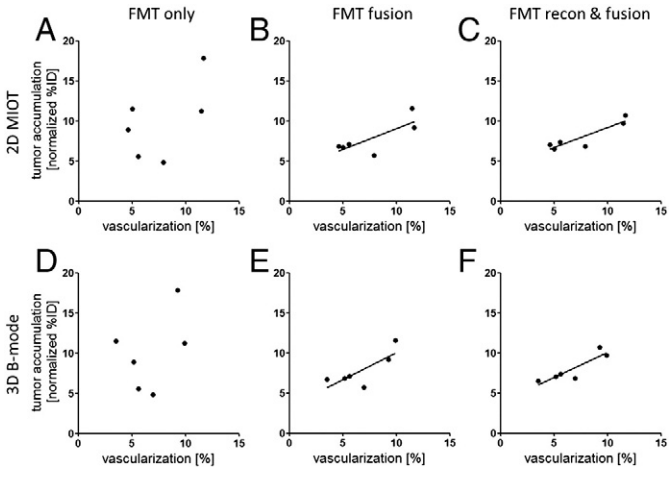

Fig. 5. Quantitative correlation of EPR-mediated passive drug targeting with tumor vascularization. The tumor accumulation of pHPMA-Dy750 was determined in six different CT26 tumor-bearing mice, and the values obtained were quantitatively correlated with the levels of tumor vascularization. EPR-mediated passive tumor targeting was evaluated using FMT (A, D), CT-FMT fusion (B, E) and CT-FMT recon & fusion (C, F). Tumor vascularization was assessed using 2D MIOT (A–C) and 3D B-mode (D–F) US imaging. The corresponding Pearson correlation coefficients and *p*-values are presented in Table 1.

Table 1
Analysis of the correlation between EPR-mediated tumor targeting and tumor vascularization.

Vascularization	Image analysis	*P*-value	r^2
2D MIOT	FMT only	0.23	0.33
2D MIOT	CT/FMT fusion	0.074	0.59
2D MIOT	CT/FMT recon & fusion	0.013	0.82
3D B-mode	FMT only	0.41	0.33
3D B-mode	CT/FMT fusion	0.069	0.6
3D B-mode	CT/FMT recon & fusion	0.019	0.78

3.3. Correlating EPR-mediated drug targeting with tumor vascularization

Subsequently, the degree of EPR-mediated tumor targeting, as assessed using FMT and CT-FMT, was correlated with the degree of tumor vascularization, as assessed using 2D MIOT and 3D B-mode US imaging. As shown in Fig. 4, as hypothesized, passive tumor targeting correlated very well with tumor vascularization. It should be noted in this regard that the fact that the absolute values for the percentage tumor vascularization (4–11%) and the percentage of the injected dose accumulating in tumors (5–12%) corresponded very closely seems to be a coincidence (not in the last place as this strongly depends on how the values for %ID accumulating in tumors are expressed; here per 250 mm^3 tumor).

Fig. 4A–H shows CT-FMT fusion images of mice presenting with low (left panels) and high (right panels) levels of passive tumor targeting. In line with this, Fig. 4I–P provide non-invasive imaging information on the degree of tumor vascularization in these two mice, exemplifying that relatively poorly vascularized tumors (rBV = 7.0% in 3D-US; Fig. 4I, J, M and N) presented with less EPR (tumor accumulation = 6.9% ID in reconstructed CT-FMT; Fig. 4A, C, E and F) than did well-vascularized tumors (rBV = 10.0% in 3D-US; Fig. 4K, L, O and P), which presented with more prominent levels of EPR (tumor accumulation = 9.7% ID in reconstructed CT-FMT; Fig. 4B, D, G and H).

When finally quantitatively comparing the levels of EPR-mediated passive drug targeting with the levels of tumor vascularization, a very good correlation was observed. As shown in Fig. 5, this was not found to be the case for 'FMT only', for which the overall levels of EPR-mediated drug targeting varied quite substantially (from 5 to 18% ID; Fig. 5A). For both hybrid CT-FMT protocols, on the other hand, the accumulation of pHPMA-Dy750 correlated very well with tumor vascularization. For 'standard' CT-FMT fusion, decent Pearson correlation coefficients and *p*-values close to statistical significance were observed. For the reconstructed CT-FMT fusion protocol, the correlation coefficients were ~0.8, and the *p*-values were <0.02 (see Table 1).

Consequently, our findings indicate that the degree of tumor vascularization might be a suitable parameter for predicting EPR. These insights are considered to be highly important for better understanding EPR, for identifying image-able (patho-) physiological parameters determining EPR, and potentially also for personalizing EPR-based nanochemotherapeutic treatments. It should be kept in mind in this regard that not only genomic and proteomic information on the expression of tumor-specific genes and proteins can be employed to individualize anticancer therapies [44,45], but that also the visualization, quantification and prediction of the target site accumulation of tumor-targeted nanomedicines might hold significant potential for personalizing antitumor treatments [46–49]. Therefore, such nanotheranostic concepts, in which drug targeting and imaging are combined, are considered to be highly useful for improving the balance between the efficacy and the toxicity of systemic anticancer therapy.

4. Conclusion

Reasoning that EPR is a highly variable phenomenon, and that some patients might really benefit from treatment with passively tumor-targeted nanomedicine formulations (via improved efficacy), while others might only profit from a reduction of drug accumulation in healthy tissues (via reduced toxicity), we have here set out to evaluate if imageable pathophysiological parameters, such as tumor vascularization, can be used to predict EPR-mediated passive drug targeting. As hypothesized, the degree of tumor vascularization correlated very well with the degree of EPR-mediated tumor accumulation (at least for ~10 nm-sized polymeric drug carriers administered to mice bearing subcutaneous CT26 tumors). To generalize this hypothesis, however, and to make these results more relevant for the clinical situation, our findings need to be confirmed in other tumor models and using other nanomedicine formulations. In addition, analogous to tumor vascularization, also other imageable parameters, such as tumor perfusion, tumor permeability and tumor cellularity, might be useful for predicting EPR-mediated passive drug targeting, and should be evaluated as potential imaging biomarkers in future studies. Nonetheless, based on the insights and evidence provided here, it seems to be justified to conclude that simple and straightforward imaging tools, such as the contrast-enhanced US-based assessment of tumor vascularization, can potentially be used to predict the efficiency of passive tumor targeting. Consequently, such theranostic concepts, in which drug targeting and imaging are intimately combined, appear to be highly useful for individualizing and improving nanomedicine-based chemotherapeutic interventions.

Supplementary data to this article can be found online at http://dx.doi.org/10.1016/j.jconrel.2014.03.007.

Acknowledgments

The authors gratefully acknowledge financial support by the European Research Council (ERC-StG-309495: NeoNaNo), by the DFG (LA 2937/1-2), by the European Union (European Regional Development Fund—Investing In Your Future; and COST-Action TD1004), by the German Federal State of North Rhine Westphalia (HighTech.NRW/EU-Ziel 2-Programm (EFRE); ForSaTum), by the Grant Agency of the Czech Republic (Grant No. P207/12/J030), and by Philips Research.

References

[1] V. Wagner, A. Dullaart, A.K. Bock, A. Zweck, The emerging nanomedicine landscape, Nat. Biotechnol. 24 (2006) 1211–1217.
[2] D. Peer, J.M. Karp, S. Hong, O.C. Farokhzad, R. Margalit, R. Langer, Nanocarriers as an emerging platform for cancer therapy, Nat. Nanotechnol. 2 (2007) 751–760.
[3] T. Lammers, W.E. Hennink, G. Storm, Tumour-targeted nanomedicines: principles and practice, Br. J. Cancer 99 (2008) 392–397.
[4] B.Y. Kim, J.T. Rutka, W.C. Chan, Nanomedicine, N. Engl. J. Med. 363 (2010) 2434–2443.
[5] R. Duncan, R. Gaspar, Nanomedicine(s) under the microscope, Mol. Pharm. 8 (2011) 2101–2141.
[6] T.M. Allen, P.R. Cullis, Liposomal drug delivery systems: from concept to clinical applications, Adv. Drug Deliv. Rev. 65 (2013) 36–48.
[7] Y. Matsumura, H. Maeda, A new concept for macromolecular therapeutics in cancer chemotherapy: mechanism of tumoritropic accumulation of proteins and the antitumor agent smancs, Cancer Res. 46 (1986) 6387–6392.
[8] H. Maeda, H. Nakamura, J. Fang, The EPR effect for macromolecular drug delivery to solid tumors: improvement of tumor uptake, lowering of systemic toxicity, and distinct tumor imaging *in vivo*, Adv. Drug Deliv. Rev. 65 (2013) 71–79.
[9] R.K. Jain, T. Stylianopoulos, Delivering nanomedicine to solid tumors, Nat. Rev. Clin. Oncol. 7 (2010) 653–664.
[10] T. Lammers, F. Kiessling, W.E. Hennink, G. Storm, Drug targeting to tumors: principles, pitfalls and (pre-) clinical progress, J. Control. Release 161 (2012) 175–187.
[11] S. Taurin, H. Nehoff, K. Greish, Anticancer nanomedicine and tumor vascular permeability; where is the missing link? J. Control. Release 164 (2012) 265–275.
[12] I.K. Kwon, S.C. Lee, B. Han, K. Park, Analysis on the current status of targeted drug delivery to tumors, J. Control. Release 164 (2012) 108–114.
[13] Y.H. Bae, K. Park, Targeted drug delivery to tumors: myths, reality and possibility, J. Control. Release 153 (2011) 198–205.
[14] T. Lammers, SMART drug delivery systems: Back to the future vs. clinical reality, Int. J. Pharm. 454 (2013) 527–529.
[15] J. Kopecek, P. Kopeckova, HPMA copolymers: origins, early developments, present, and future, Adv. Drug Deliv. Rev. 62 (2010) 122–149.
[16] T. Lammers, K. Ulbrich, HPMA copolymers: 30 years of advances, Adv. Drug Deliv. Rev. 62 (2010) 119–121.
[17] H. Maeda, Tumor-selective delivery of macromolecular drugs via the EPR effect: background and future prospects, Bioconjug. Chem. 21 (2010) 797–802.
[18] P.A. Vasey, S.B. Kaye, R. Morrison, C. Twelves, P. Wilson, R. Duncan, A.H. Thomson, L. S. Murray, T.E. Hilditch, T. Murray, S. Burtles, D. Fraier, E. Frigerio, J. Cassidy, Phase I clinical and pharmacokinetic study of PK1 [N-(2-hydroxypropyl)methacrylamide copolymer doxorubicin]: first member of a new class of chemotherapeutic agents-drug-polymer conjugates. Cancer Research Campaign Phase I/II Committee, Clin. Cancer Res. 5 (1999) 83–94.
[19] K.J. Harrington, S. Mohammadtaghi, P.S. Uster, D. Glass, A.M. Peters, R.G. Vile, J. S. Stewart, Effective targeting of solid tumors in patients with locally advanced cancers by radiolabeled pegylated liposomes, Clin. Cancer Res. 7 (2001) 243–254.
[20] D.J. Crommelin, A.T. Florence, Towards more effective advanced drug delivery systems, Int. J. Pharm. 454 (2013) 496–511.
[21] L.W. Seymour, D.R. Ferry, D.J. Kerr, D. Rea, M. Whitlock, R. Poyner, C. Boivin, S. Hesslewood, C. Twelves, R. Blackie, A. Schatzlein, D. Jodrell, D. Bissett, H. Calvert, M. Lind, A. Robbins, S. Burtles, R. Duncan, J. Cassidy, Phase II studies of polymer-doxorubicin (PK1, FCE28068) in the treatment of breast, lung and colorectal cancer, Int. J. Oncol. 34 (2009) 1629–1636.
[22] R. Duncan, Polymer conjugates as anticancer nanomedicines, Nat. Rev. Cancer 6 (2006) 688–701.
[23] R. Duncan, Development of HPMA copolymer-anticancer conjugates: clinical experience and lessons learnt, Adv. Drug Deliv. Rev. 61 (2009) 1131–1148.
[24] L.W. Seymour, D.R. Ferry, D. Anderson, S. Hesslewood, P.J. Julyan, R. Poyner, J. Doran, A.M. Young, S. Burtles, D.J. Kerr, Hepatic drug targeting: phase I evaluation of polymer-bound doxorubicin, J. Clin. Oncol. 20 (2002) 1668–1676.
[25] F. Kiessling, M. Heilmann, T. Lammers, K. Ulbrich, V. Subr, P. Peschke, B. Waengler, W. Mier, H.H. Schrenk, M. Bock, L. Schad, W. Semmler, Synthesis and characterization of HE-24.8: a polymeric contrast agent for magnetic resonance angiography, Bioconjug. Chem. 17 (2006) 42–51.
[26] T. Lammers, V. Subr, P. Peschke, R. Kuhnlein, W.E. Hennink, K. Ulbrich, F. Kiessling, M. Heilmann, J. Debus, P.E. Huber, G. Storm, Image-guided and passively tumour-targeted polymeric nanomedicines for radiochemotherapy, Br. J. Cancer 99 (2008) 900–910.
[27] Z.R. Lu, Molecular imaging of HPMA copolymers: visualizing drug delivery in cell, mouse and man, Adv. Drug Deliv. Rev. 62 (2010) 246–257.
[28] T. Lammers, V. Subr, K. Ulbrich, W. Hennink, G. Storm, F. Kiessling, Polymeric nanomedicines for image-guided drug delivery and tumor-targeted combination therapy, NanoToday 5 (2010) 197–212.
[29] S. Kunjachan, R. Pola, F. Gremse, B. Theek, J. Ehling, D. Moeckel, B. Hermanns-Sachweh, M. Pechar, K. Ulbrich, W.E. Hennink, G. Storm, W. Lederle, F. Kiessling, T. Lammers, Passive versus active tumor targeting using RGD- and NGR-modified polymeric nanomedicines, Nano Lett. 14 (2014) 972–981.
[30] R.B. Schulz, A. Ale, A. Sarantopoulos, M. Freyer, E. Soehngen, M. Zientkowska, V. Ntziachristos, Hybrid system for simultaneous fluorescence and x-ray computed tomography, IEEE Trans. Med. Imaging 29 (2010) 465–473.
[31] A. Ale, V. Ermolayev, E. Herzog, C. Cohrs, M.H. de Angelis, V. Ntziachristos, FMT-XCT: *in vivo* animal studies with hybrid fluorescence molecular tomography-X-ray computed tomography, Nat. Methods 9 (2012) 615–620.
[32] S. Kunjachan, F. Gremse, B. Theek, P. Koczera, R. Pola, M. Pechar, T. Etrych, K. Ulbrich, G. Storm, F. Kiessling, T. Lammers, Noninvasive optical imaging of nanomedicine biodistribution, ACS Nano 7 (2013) 252–262.
[33] F. Kiessling, S. Fokong, P. Koczera, W. Lederle, T. Lammers, Ultrasound microbubbles for molecular diagnosis, therapy, and theranostics, J. Nucl. Med. 53 (2012) 345–348.
[34] J. Ehling, T. Lammers, F. Kiessling, Non-invasive imaging for studying anti-angiogenic therapy effects, Thromb. Haemost. 109 (2013) 375–390.
[35] S. Fokong, M. Siepmann, Z. Liu, G. Schmitz, F. Kiessling, J. Gatjens, Advanced characterization and refinement of poly N-butyl cyanoacrylate microbubbles for ultrasound imaging, Ultrasound Med. Biol. 37 (2011) 1622–1634.
[36] J.L. Tremoleda, A. Kerton, W. Gsell, Anaesthesia and physiological monitoring during *in vivo* imaging of laboratory rodents: considerations on experimental outcomes and animal welfare, EJNMMI Res. 2 (2012) 44.
[37] F. Gremse, V. Schulz, Qualitative and Quantitative Data Analysis, in: F. Kiessling, B. Pichler (Eds.), Small Animal Imaging, Springer, Berlin Heidelberg, 2011, pp. 363–378.
[38] M. Palmowski, W. Lederle, J. Gaetjens, M. Socher, P. Hauff, J. Bzyl, W. Semmler, R.W. Gunther, F. Kiessling, Comparison of conventional time-intensity curves vs. maximum intensity over time for post-processing of dynamic contrast-enhanced ultrasound, Eur. J. Radiol. 75 (2010) e149–e153.
[39] A. Rix, W. Lederle, M. Siepmann, S. Fokong, F.F. Behrendt, J. Bzyl, C. Grouls, F. Kiessling, M. Palmowski, Evaluation of high frequency ultrasound methods and contrast agents for characterising tumor response to anti-angiogenic treatment, Eur. J. Radiol. 81 (2012) 2710–2716.
[40] Q. Zhang, H. Yang, S.J. Kang, Y. Wang, G.D. Wang, T. Coulthard, H.E. Grossniklaus, In vivo high-frequency, contrast-enhanced ultrasonography of uveal melanoma in mice: imaging features and histopathologic correlations, Invest. Ophthalmol. Vis. Sci. 52 (2011) 2662–2668.
[41] K. Licha, C. Olbrich, Optical imaging in drug discovery and diagnostic applications, Adv. Drug Deliv. Rev. 57 (2005) 1087–1108.

[42] M. Liong, J. Lu, M. Kovochich, T. Xia, S.G. Ruehm, A.E. Nel, F. Tamanoi, J.I. Zink, Multifunctional inorganic nanoparticles for imaging, targeting, and drug delivery, ACS Nano 2 (2008) 889–896.
[43] J. Gao, K. Chen, R. Luong, D.M. Bouley, H. Mao, T. Qiao, S.S. Gambhir, Z. Cheng, A novel clinically translatable fluorescent nanoparticle for targeted molecular imaging of tumors in living subjects, Nano Lett. 12 (2012) 281–286.
[44] M.A. Hamburg, F.S. Collins, The path to personalized medicine, N. Engl. J. Med. 363 (2010) 301–304.
[45] L. Chin, J.N. Andersen, P.A. Futreal, Cancer genomics: from discovery science to personalized medicine, Nat. Med. 17 (2011) 297–303.
[46] T. Lammers, S. Aime, W.E. Hennink, G. Storm, F. Kiessling, Theranostic nanomedicine, Acc. Chem. Res. 44 (2011) 1029–1038.
[47] T. Lammers, L.Y. Rizzo, G. Storm, F. Kiessling, Personalized nanomedicine, Clin. Cancer Res. 18 (2012) 4889–4894.
[48] S. Mura, P. Couvreur, Nanotheranostics for personalized medicine, Adv. Drug Deliv. Rev. 64 (2012) 1394–1416.
[49] L.Y. Rizzo, B. Theek, G. Storm, F. Kiessling, T. Lammers, Recent progress in nanomedicine: therapeutic, diagnostic and theranostic applications, Curr. Opin. Biotechnol. 24 (2013) 1159–1166